Supplementary Information

Huge magnetoresistance and ultra-sharp metamagnetic transition in polycrystalline $Sm_{0.5}Ca_{0.25}Sr_{0.25}MnO_3$

Sanjib Banik[1], Kalipada Das[1,2], Tapas Paramanik[1,3], N. P. Lalla[4], Biswarup Satpati[5], K. Pradhan[1+], and I. Das[1*]

[1] CMP Division, Saha Institute of Nuclear Physics, HBNI, 1/AF-Bidhannagar, Kolkata 700 064, India

[2] Department of Physics, Seth Anandram Jaipuria College, 10-Raja Naba Krishna Street, Kolkata-700005, India

[3] Indian Institute of Technology, Kharagpur- 721302, India

[4] UGC-DAE Consortium for Scientific Research, University Campus, Khandwa Road, Indore-452017, India

[5] Surface Physics and Material Science Division, Saha Institute of Nuclear Physics, HBNI, 1/AF-Bidhannagar, Kolkata 700 064, India

I. EXPERIMENTAL WORK

A. X-ray diffraction study

The room temperature XRD data has been profile fitted using Pnma space group and shows the single phase nature of the sample with orthorhombic structure. The low temperature data has also been tried to fit with single Pnma space group but does not give satisfactory fitting. Previously it was reported that $Sm_{0.5}Sr_{0.5}MnO_3$ sample undergoes crystallographic phase coexistence at low temperature with monoclinic P21/m symmetry[1]. Since the present sample is in between $Sm_{0.5}Ca_{0.5}MnO_3$ and $Sm_{0.5}Sr_{0.5}MnO_3$, we had tried to fit the low temperature (15 K) XRD data with P21/m but it also does not give any satisfactory fitting. Finally, fitting with Pnma+P21/m gives the best fit. We present the extracted lattice parameters in Table. I.

TABLE I. The lattice parameters and unit cell volumes of the sample $Sm_{0.5}Ca_{0.25}Sr_{0.25}MnO_3$

Temperature (K)	Space group	a ($\AA$)	b ($\AA$)	c ($\AA$)	V ($\AA^3$)	
300	Pnma	5.395	7.611	5.408	222.049	
15	Pnma + P21/m	5.456	7.618	5.384	223.804	Pnma
15	Pnma + P21/m	5.380	10.849	7.569	441.802	P21/m

B. HRTEM study

A typical TEM image of a crystallite of the sample has been presented in Fig. 1(a). In the marked portion electron diffraction pattern has been taken which has been shown in the Fig. 1 (e) of the main text. The HRTEM image of the sample at room temperature is presented in Fig. 1(b) and Fig. 1(c) is the magnified view of the small domain. It shows the change in contrast due to the segregation of different atoms in the atomic scale. The interplanar spacing has been shown in the figure. Here another point needs to mention that the error bar in determining the interplanar spacing in the figure is $\pm 0.04\AA$ [2].

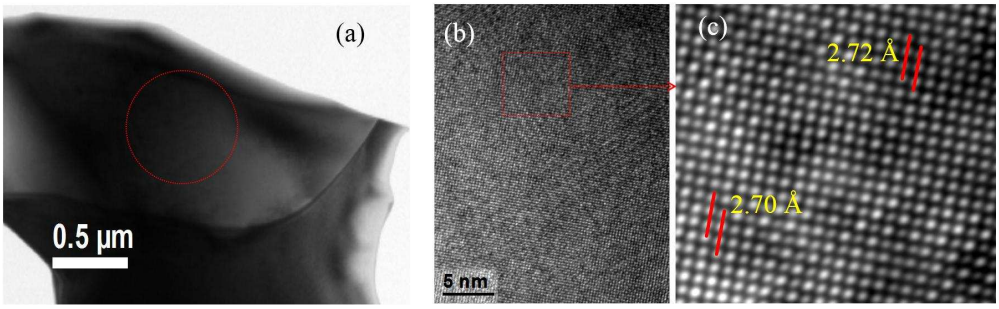

FIG. 1. Panel (a) gives a typical TEM overview of one crystallite where two grains are visible. Panel (b) gives a typical HRTEM overview of one crystallite. Panel (c) [a magnified view of tiny domains in (b)] displays an example of atomic scale variation of the contrast.

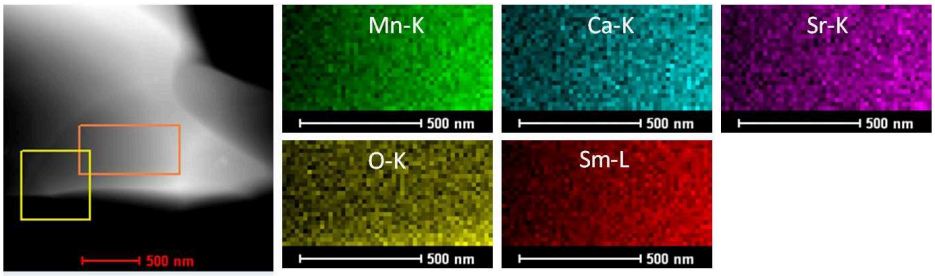

FIG. 2. STEM-HAADF image and corresponding drift corrected chemical maps from the area marked by orange box in left panel.

C. EDS Analysis

The EDS analysis in scanning transmission electron microscopy high angle annular dark field (STEM-HAADF) mode was carried out with a ∼2 nm probe and shows that the crystal is having highly homogeneous distribution of elements [Fig. 2]. The chemical analysis (see Table. II) confirms the stoichiometric nature of the compound.

D. Thermoremanent magnetization measurements

Thermoremanent magnetization measurements were carried out by the following protocol: the sample was cooled down from the room temperature in the presence of 100 Oe external magnetic field and the magnetization data was recorded (denoted by 100 Oe FCC in Fig. 3). The 100 Oe FCC data indicates the presence of very small fraction of ferromagnetic phase. After reaching the specified temperature (T = 2 K), magnetic field increases from 100 Oe

TABLE II. The EDS analysis of the sample $Sm_{0.5}Ca_{0.25}Sr_{0.25}MnO_3$

Element	Atomic %
O (K)	59.39
Ca (K)	4.94
Mn (K)	20.43
Sr (K)	5.71
Sm (L)	9.50

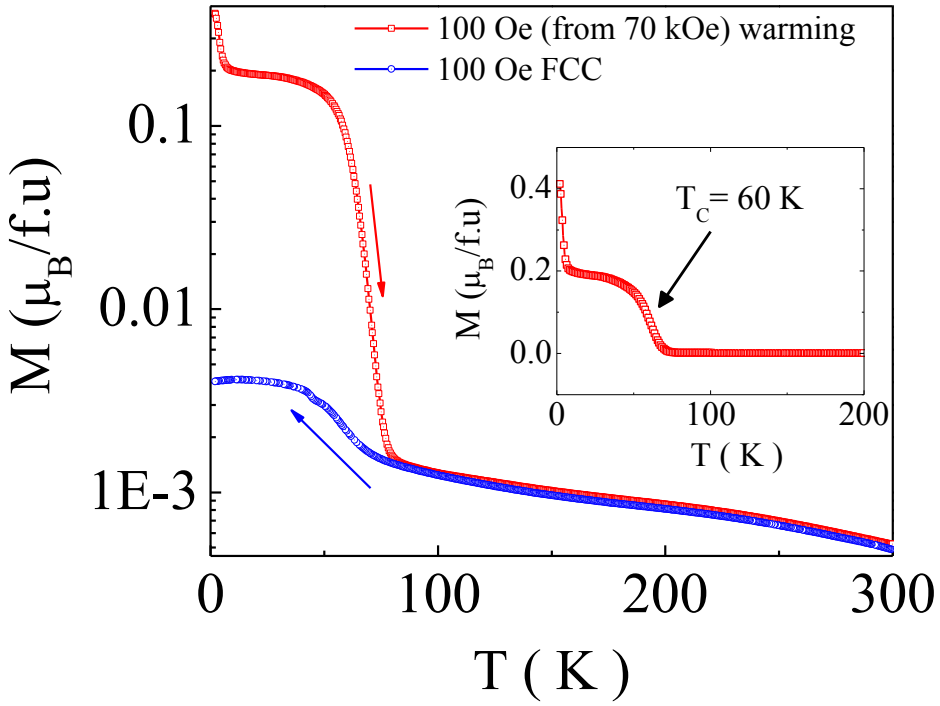

FIG. 3. Magnetization as a function of temperature measures at H = 100 Oe external magnetic field. Blue curve is the magnetization during cooling of the sample (at H = 100 Oe). Red curve (linear scale in the inset) is magnetization during warming in the presence of H = 100 Oe external magnetic field (before starting measurements (at T = 2 K) the field cycled from 100 Oe to 70 kOe to 100 Oe).

to 70 kOe and stayed for some time (approximately 5 mins). After that magnetic field was reduced to 100 Oe and magnetization data was recorded during warming cycle (see Fig. 3). During the warming cycle the system changes to a paramagnetic phase at 60 K.

E. Heat Capacity Measurements

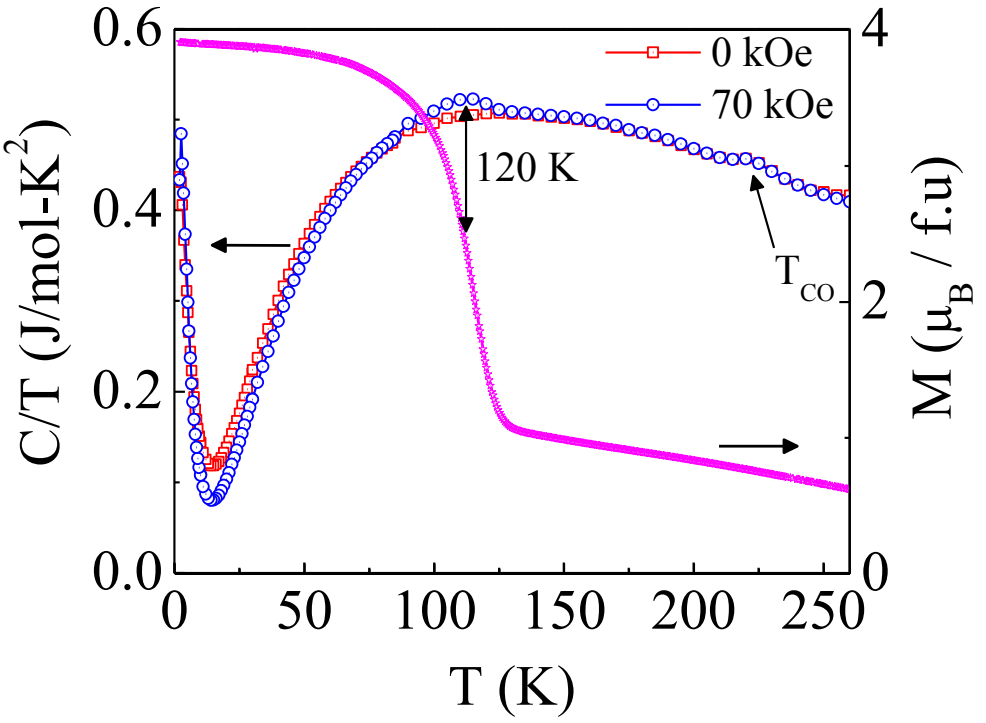

FIG. 4. Left axes: C/T as a function of temperature (C is heat capacity) in the absence and in the presence of 70 kOe external magnetic field. Right axes: Temperature dependence of the magnetization measured in presence of 70 kOe magnetic field.

Around 120 K, magnetization data measured at 70 kOe field also shows a sharp increase like paramagnetic to ferromagnetic transition [see Fig.4]. Thus the kink at 120 K in the heat capacity is associated with the paramagnetic to ferromagnetic transition. Though in the virgin sample around 120 K there is an antiferromagnetic transition as observed from the derivative of M(T) data in 100 Oe field. Therefore, it can be concluded that 70 kOe field converts the AFM fraction to FM phase which results in the rise in the peak in C/T versus T data (see Fig. 4). Additionally, the sharper increasing nature of C/T below 15 K is observed which is due to the magnetic ordering of Sm^{3+} ions[3, 4].

F. Sweep rate dependent magnetization

Isothermal magnetization (at 2 K) has been measured in ZFC mode for different field sweep rate (10 Oe/sec and 200 Oe/sec) and the corresponding plot is presented in Fig. 5. For lowest sweep rate (10 Oe/sec) jump occurs at higher field compared to that of the maximum sweep rate. For lower sweep rate lattice has adequate time to accommodate the induced interfacial strain between AF and FM domains but for higher sweep rate strain propagates rapidly and conversion to FM phase take place. This scenario indicates the martensitic nature of the transition.

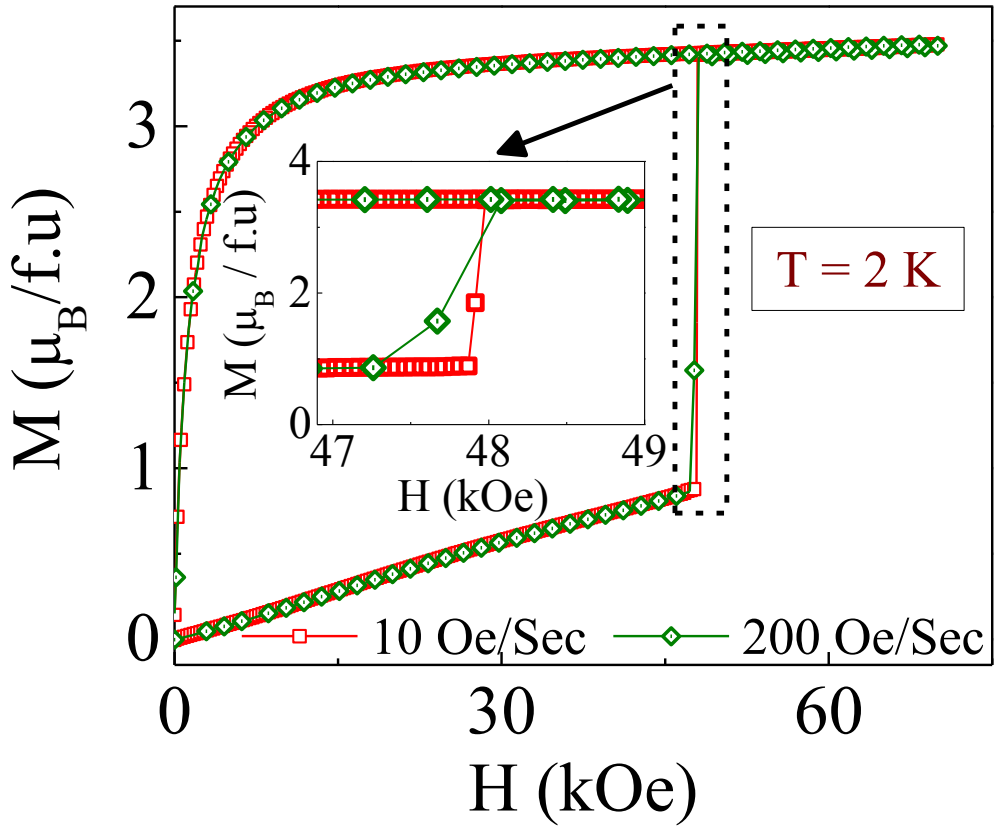

FIG. 5. Isothermal magnetization as a function of external magnetic field at 2 K temperature for different field sweep rate 10 Oe/sec and 200 Oe/sec.

G. Resistivity Relaxation study at 25 K

To investigate the dynamics of the resistivity jumps we performed resistivity relaxation measurements at T = 25 K (sample was ZFC from room temperature down to 25 K) by applying three different magnetic fields (H_1, H_2, H_3) smaller than the H_{CR} as shown in Fig.6. Resistivity of the sample as a function of time shows resistivity jumps at different incubation time. The *incubation time*, time spent before the jumps, increases from ∼20 Sec to ∼1000 Sec with decrease in the applied magnetic field. For the fixed temperature (25 K), with decrease in the applied magnetic field the elastic barrier height (arises due to the lattice strain at low temperature discussed earlier) increases and for that reason system needs more *incubation time* to overcome the elastic barrier for burst-like growth of the ferromagnetic fractions in the expense of the antiferromagnetic components. This type of relaxation behavior is generally the characteristics of standard martensitic transformations[5–9].

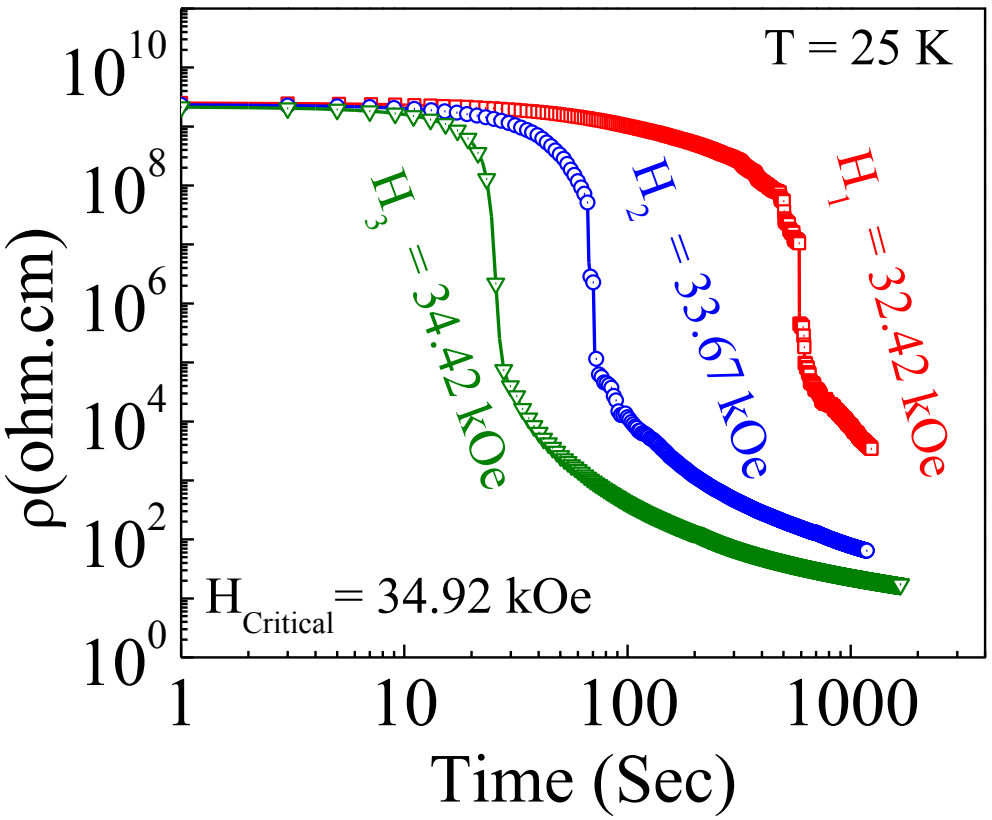

FIG. 6. Evolution of resistivity with time at 25 K for different applied magnetic fields (H_1, H_2, H_3) such that $H_1 < H_2 < H_3 < H_{CR}$.

II. MODEL HAMILTONIAN AND METHOD

We consider following two-band double-exchange model [10] for e_g electrons, Hund's coupled to t_{2g} (Mn core spins) in a square lattice:

$$H = -\sum_{\langle ij\rangle\sigma}^{\alpha\beta} t_{\alpha\beta}^{ij} c_{i\alpha\sigma}^{\dagger} c_{j\beta\sigma} \; - J_H \sum_i \mathbf{S}_i.\boldsymbol{\sigma}_i \\ + J_{AF} \sum_{\langle ij\rangle} \mathbf{S}_i.\mathbf{S}_j - \lambda \sum_i \mathbf{Q}_i.\boldsymbol{\tau}_i + \frac{K}{2}\sum_i \mathbf{Q}_i^2 + \sum_i (\epsilon_i - \mu) n_i. \quad (1)$$

Here, c ($c^{\dagger}$) is the annihilation (creation) operator for e_g electrons and α, β are the two Mn-e_g orbitals $d_{x^2-y^2}$ and $d_{3z^2-r^2}$. $t_{\alpha\beta}^{ij}$ are hopping amplitudes between nearest-neighbor sites in x and y directions: $t_{aa}^x = t_{aa}^y \equiv t$, $t_{bb}^x = t_{bb}^y \equiv t/3$, $t_{ab}^x = t_{ba}^x \equiv -t/\sqrt{3}$, $t_{ab}^y = t_{ba}^y \equiv t/\sqrt{3}$. $J_{\rm H}$ is the Hund's coupling between $e_{\rm g}$ electron spin σ_i and $t_{2\rm g}$ spin $\mathbf{S}_{\rm i}$ at site i. The $e_{\rm g}$ electrons are also coupled to Jahn-Teller phonons $\mathbf{Q}_{\rm i}$ by λ. J is antiferromagnetic super-exchange coupling between the $t_{2\rm g}$ spins. We treat $\mathbf{S}_{\rm i}$ and $\mathbf{Q}_{\rm i}$ as classical variables [11, 12] and adopt the double-exchange limit [10] , i.e. $J_H \to \infty$. We set K (stiffness of Jahn-Teller modes) and $|\mathbf{S}_{\rm i}|$ to be 1. This well studied model Hamiltonian qualitatively reproduces the phase diagram of manganites. The chemical potential μ is adjusted to fix the the electron density at 0.5. We include effect of disorder by adding $\sum_i \epsilon_i n_i$ term to the Hamiltonian, where ϵ_i is the quenched disorder potential.

We applied Monte-Carlo simulation to the classical variables $\mathbf{S}_{\rm i}$ and $\mathbf{Q}_{\rm i}$, and an exact diagonalization scheme is employed to the fermionic sector (e_g electrons). We used travelling cluster approximation (TCA) [13] based Monte-Carlo to handle large system size (24×24 lattice). We annealed the randomized classical spins $\mathbf{S}_i$ and lattice distortions $\mathbf{Q}_i$ in an arbitrary quenched disorder configuration, and anneal down from temperature $T = 0.1t$ (t is the hopping parameter). The resistivity, in units of $\hbar a/\pi e^2$ (a: lattice constant) is obtained by calculating the dc limit of the conductivity using the Kubo-Greenwood formalism [14, 15]. The magnetic structure factor at wave vector $\mathbf{q} = (0, 0)$ is calculated from $S(\mathbf{q}) = \frac{1}{N^2} \sum_{ij} \mathbf{S_i} \cdot \mathbf{S_j}\ \mathrm{e}^{i\mathbf{q}\cdot(\mathbf{r_i}-\mathbf{r_j})}$. Physical quantities, i.e. resistivity are averaged over ten different disorder

configurations in addition to the thermal averages taken during the Monte Carlo simulations.

[1] Kurbakov, A. I., Lazuta, A. V. & Ryzhov, V. A., Phase diagram of $Sm_{1-x}Sr_xMnO_3$ perovskite manganites. J. Phys. Conf. Ser. **200**, 012099 (2010).

[2] Satpati, B., Satyam, P. V., Som, T. & Dev, B. N. Nanoscale ion-beam mixing in Au-Si and Ag-Si eutectic systems. Appl. Phys. A Mater. Sci. Process. **79**, 447-451 (2004).

[3] OFlynn, D., Tomy, C. V., Lees, M. R., Daoud-Aladine, A. & Balakrishnan, G. Multiferroic properties and magnetic structure of $Sm_{1-x}Y_xMnO_3$. Phys. Rev. B **83**, 174426 (2011).

[4] Midya, A., Das, S. N., Mandal, P., Pandya, S. & Ganesan, V. Anisotropic magnetic properties and giant magnetocaloric effect in antiferromagnetic $RMnO_3$ crystals (R = Dy, Tb, Ho, and Yb). Phys. Rev. B **84**, 235127 (2011).

[5] Maji, B., Suresh, K. G. & Nigam, A. K. Observation of spontaneous magnetization jump and field-induced irreversibility in Nd_5Ge_3. Europhys. Lett. **91**, 37007 (2010).

[6] Liao, D., Sun, Y., Yang, R., Li, Q. & Cheng, Z. Spontaneous magnetization and resistivity steps in the bilayered manganite $(La_{0.5}Nd_{0.5})_{1.2}Sr_{1.8}Mn_2O_7$. Phys. Rev. B **74**, 174434 (2006).

[7] Wu, T. & Mitchell, J. F. Magnetization steps in manganite films:Time delay of the metamagnetic transition. Phys. Rev. B **69**, 100405 (2004).

[8] Shankaraiah, N., Murthy, K. P. N., Lookman, T. & Shenoy, S. R. Incubation times and entropy barriers in martensitic kinetics: Monte Carlo quench simulations of strain pseudospins. Europhys. Lett. **92**, 36002 (2010).

[9] Hardy, V. et al. Observation of spontaneous magnetization jumps in manganites. Phys. Rev. B **68**, 220402 (2003).

[10] Dagotto, E., Hotta, T. & Moreo, A. Colossal magnetoresistant materials: the key role of phase separation. Phys. Rep. **344**, 1-153 (2001).

[11] Yunoki, S., Hu, J., Malvezzi, A. L., Moreo, A., Furusaki, N. & Dagotto, E. Phase separation in electronic models for manganites Phys. Rev. Lett. **80**, 845 (1998).

[12] Dagotto, E., Yunoki, S., Malvezzi, A. L., Moreo, A., Hu, J., Capponi, S., Poilblanc, D. & Furukawa, N. Ferromagnetic Kondo model for manganites: Phase diagram, charge segregation, and influence of quantum localized spins. Phys. Rev. B **58**, 6414 (1998).

[13] Kumar, S. & Majumdar, P. A travelling cluster approximation for lattice fermions strongly

coupled to classical degrees of freedom. Eur. Phys. J. B **50**, 571 (2006).

[14] Mahan, G. D., *Quantum Many Particle Physics* (Plenum Press, New York, 1990).

[15] Kumar, S. & Majumdar, P. Anti-localisation to strong localisation: The interplay of magnetic scattering and structural disorder. Europhys. Lett. **65**, 75 (2004).